MEASUREMENT OF THE PHOTORECEPTOR POINTING IN THE LIVING CHICK EYE

A thesis presented to the graduate faculty of
New England College of Optometry in partial fulfillment
of the requirements for the degree of Master of Science

Maria K. Walker

May 17, 2013

© Maria K. Walker
All rights reserved

The author hereby grants New England College of Optometry permission to reproduce and to distribute publicly paper and electronic copies of the thesis document in whole or in part.

MEASUREMENT OF THE PHOTORECEPTOR POINTING IN THE LIVING CHICK EYE

Maria K. Walker

This manuscript has been read and accepted by the
Thesis Committee in satisfaction of the
thesis requirement for the degree of Master of Science

5/17/13
Date

Nathan Doble, Ph.D.
Graduate Faculty Advisor

Elise N. Harb, O.D., M.S.
Thesis Committee Member

Frances Rucker, M.C.Optom., Ph.D.
Thesis Committee Member

Radouil Tzekov, M.D., Ph.D.
Thesis Committee Member

5-17-13
Date

Nancy J. Coletta, O.D., Ph.D.
Director of Graduate Studies

New England College of Optometry

MEASUREMENT OF THE PHOTORECEPTOR POINTING IN THE LIVING CHICK EYE

Maria K. Walker
New England College of Optometry, 2013

Abstract

Purpose:

The chick is a widely used animal model in the study of eye growth, in particular for emmetropization and myopia. Like most eyes, the ability to image the fine retinal structure is degraded by the aberrations in the lens and cornea. These aberrations have therefore required sacrificing the animal and employing histological analysis to determine the precise retinal changes that occur when a change such as myopic induction is applied. The work described here uses adaptive optics (AO) to overcome the ocular aberration allowing for cellular level imaging in-vivo. In particular, we utilize this imaging capability to examine the cone waveguide directionality of individual chick photoreceptors.

Methods:

White Leghorn chickens (*Gallus gallus* domesticus) (age 48d, approx. 650g) were anesthetized with a combination of Ketamine/Xylazine and dilated with vecuronium bromide suspension prior to imaging. The AO fundus camera at the New England College of Optometry was modified in order to image the smaller 3mm pupil of the chick. By translating the entrance pupil position of the imaging beam (650nm wavelength) on the

corneal surface, the direction of the imaging light is varied allowing for the measurement of the individual cone pointing. The same retinal location (1-degree field of view) was imaged under the thirteen entrance pupil positions with four retinal images being registered together for each position. Upon compensating for the variation in imaging light intensity due to light delivery optics, a curve fitting algorithm was used to determine the directionality of the individual cones.

Results:

Fourteen retinal images were taken of chick A and chick B in order to measure the cone directionality. The luminance change seen in the images as the entrance beam moves away from the central pupil represents the decreased cone response to light rays entering the pupil at oblique axes. In both chicks, we see disarray among the cones' directionality; however, this disarray is ultimately quite small. Our images show a narrow distribution of cone pointing (ρ values: chick A: 0.076; chick B: 0.063), and we find that all retinal cones generally point toward the same general location on the pupil, slightly superior to the pupil center, in agreement with a previous ERG experiment on chicks.

Conclusion:

Similar to the human eye, the chick photoreceptor disarray is small, implying that the receptors are aligned to maximize the signal coming through the center of the pupil aperture.

Acknowledgements

This research was supported by the National Eye Institute T35 summer research grant program. I would like to thank Dr. Debora Nickla and Kristen Totonelly and for their assistance with chicks, as well as training with the ultrasound and refractive error measurements. I acknowledge the help of Drs. Leonardo Blanco and Susanna Finn, and also Robert Flores for their help with the Matlab scripts. I thank Rebecca Kivlin and Jennifer Choi for their assistance with the imaging procedure, and Drs. Rad Tzekov and Stacey Choi for their helpful advice.

Commercial Relationships: N. Doble is founder of Iris AO Inc.

Presentations and Publications

Presentation:

Walker MK, Blanco L, Kivlin R and Doble N. *Measurement of the photoreceptor pointing in the living chick eye*. Presented at the Association for Research in Vision and Ophthalmology Annual Meeting (ARVO) 2013 May 5-9th; Seattle, WA.

Journal Manuscript:

Walker MK, L. Blanco, Kivlin R and Doble N. *Measurement of the photoreceptor pointing in the living chick eye*. Manuscript being prepared for Vision Research. May 2013 submission.

Table of Contents

Abstract iii

Acknowledgments v

Presentations vi

Table of Contents vii

List of Figures ix

List of Tables xiii

Introduction 1

Structure of the Chick Eye and Photoreceptor Cells 4

The Stiles Crawford Effect of the First Kind (SCE-I) 8

Previous Study Measuring Cone Directionality in Humans using AO 10

Measurement of the SCE-I in the Living Chick Eye using ERG Recording 11

The Need for Adaptive Optics 12

Methods

Animals 21

Chick mounting stage 22

AO System Modifications 23

Cone Directionality Imaging 26

Post-Processing using MATLAB 29

Results and Analysis

Effects of AO correction 30

Cone directionality results 33

Discussion **39**

Comparison with Other Chick Studies 40

Conclusion 42

References 43

Appendix 47

List of Figures

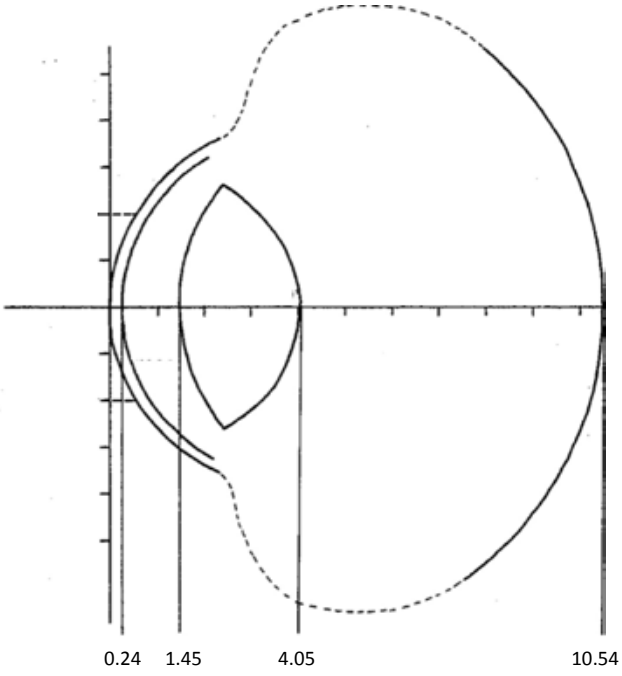

Optical Tissue	Refractive index
Cornea	1.373
Aqueous Humor	1.335
Lens	1.37-1.43
Homogenous lens model	1.455
Vitreous Humor	1.335

Optical Interface	Radius of Curvature
Anterior Cornea	3.84
Anterior Lens	4.00
Posterior Lens	-2.90
Front of Retina	-7.30

Focal length (mm)	8.5
Pupil Size (mm)	3.5
Optical power (D)	~115

Figure 1 (A) A schematic of a 30-day old chick eye [27]; the numbers directly below the schematic layout indicate the distance in mm from the anterior surface of the cornea. Corneal thickness = 0.24mm; anterior chamber depth = 1.21mm; lens thickness = 2.60mm; Vitreous humor depth = 6.49mm; axial length = 10.54mm. (B) The refractive indices and radii of curvature of the ocular media in the 30 D old chick eye [27]. The focal length of the 30D old chick eye is approx. 8.5mm and the dilated pupil diameter is about 3.5mm. The total optical power of the adult chick eye is ~115D.

Figure 2: Chick photoreceptor cell schematic of rods and the 5 spectrally distinct cone types [32].

Figure 3: Spectral sensitivities of the various cone types in the chicken and human retina [34]. The top graph shows the spectral sensitivities of the 5 different chick cone types, whose sensitivities range from 300-700 nm (VS: very short; S: short; M: middle; D: double; L: long wavelength sensitive). The spectral sensitivities of the 3 distinct human cones are seen in the bottom graph (S: short; M: middle; and L: long wavelength sensitive), and range from 400-700nm.

Figure 4: Effect of aberrations on the wavefront profile and far field point spread function (PSF) (A) The un-aberrated case gives a flat wavefront and the characteristic Airy disk pattern PSF (B) (C) Typical profile for a normal human eye. A SR > 0.80 is said to be diffraction limited. 6mm pupil diameter, 650 nm measurement wavelength.

Figure 5: The principle of adaptive optics. The deformable mirror receives incoming aberrated light reflected off of the retina. This light is also captured by the WFS, which senses the aberrations and signals the DM to adjust the mirrors to a conjugate wavefront formation. The aberrated light from the retina is then corrected during reflection off the DM and continues on to form a clear, un-aberrated image on the camera. Furthermore, the system runs on a real time loop, the pistons adjusting dynamically as they receive continuous input from the wavefront sensor.

Figure 6: Principle of the Hartmann-Shack WFS. (A) the incident pupil shown with the gray circle is sampled by a two dimensional array of lenslets. (B) Cross section through the (A). For the reference wavefront shown by the gray hatched line a focal spot is formed by each lenslet on the camera plane and is exactly centered behind each lenslet. For an aberrated wavefront (solid gray line) variations in the slope between each lenslet will cause the focal spots to be shifted from the position of the reference. By determining both the Δx and Δy shifts for each lenslet the aberrated wavefront may be reconstructed. It is important that the WFS samples the incident wavefront with sufficient speed (20-30Hz) to accurately track any temporal changes.

Figure 7: Deformable mirror types. (A) Continuous face sheet – a continuous mirror surface is deformed by an underlying array of actuators. (B) The mirror surface is composed of a discrete array of segments each of which may move in a pure piston (vertical) motion only. (C) Similar to (B) but each segment may now also move in tip and tilt in addition to piston. This is the type of DM employed for the work described here.

Figure 8: (A) One of the DM segments, which is bound to a piston-like platform that allows for axial as well as tip/tilt movements. (B) The 37 mirror segments are arranged into an array to form the overall DM surface.

Figure 9: The original optical layout of the Adaptive Optics Fundus Camera at The New England College of Optometry, with the added lens modifications for imaging chick eyes. The modifications made to the system are lens 15 and 16 along with the mirror that translates the light downward.

Figure 10: A 1° FOV fundus image of chick B, taken using the AO fundus camera at NECO (imaging beam 650nm). The image is a registered sum of 4 raw images. The illuminated areas represent reflections from cone cells in a live 48-day old White Leghorn chicken.

Figure 11: The stage used during the imaging procedure. (A) Bite bar used to position the beak of the bird. (B) rotation control for the bite bar (C) translation stage (D) axial fine translation control (knob). (E) control for fine translation along the x-axis (F) control for fine translation along the y-axis. (G) x-axis gross translation control (H) y-axis gross translation control. (I) platform used to hold the body of the bird.

Figure 12: The chick eye was translated on an x and y axis in order to change the location of the entrance beam and create an oblique entrance angle. The same retinal cones were imaged at each entrance pupil position.

Figure 13: A diagram of the entrance pupil locations used during the imaging procedure. By translating and rotating the bird eye, we imaged the retinal cones through 13 different entrance pupil locations. There were 14 total batches of image collection (13 unique + 1 additional central point) through the 3 mm chick pupil. Each point on the figure represents the amount of translation in the pupil plane for each entrance beam location.

Figure 14: Before and after AO wavefront and PSF plots for chick B. The improvement in optical quality after correction (B and D) sets the condition for the high resolution imaging of the retina. The RMS error before AO correction was 0.96um with a PV error of 4.4um and Strehl ratio (SR) of 0.02. After correction with AO, the RMS error decreased to 0.06um with a PV error of 0.41um and Strehl ratio (SR) of 0.70.

Figure 15: The retinal images taken from Chick A at 13 different pupil locations. Each image is the sum of 4 registered images. The numbers in parenthesis represent the axis position of the goniometer translation stage relating to the entrance position of the imaging light. Based on the positioning of the bird, the entrance pupil positions were superior, inferior, nasal, or

temporal on the bird as shown by the key. The luminance changes that are seen as the entrance beam moves away from the central pupil represents the decreased cone response to light rays entering the pupil at oblique axes. The intensities for each plot has been normalized to illustrate the change in brightness of the image as the entrance pupil position moves away from the peak coupling.

Figure 16: The retinal image of chick A, showing the deviation from the ensemble average for each individual cone. The red circle represents the cone with the direction and length of the line showing the angle and magnitude respectively.

Figure 17: The pupil intercept graph of Chick A, which show a fairly narrow distribution of pupil locations, indicate the points of the pupil that each cone would reflect light through based on their directional positioning. This plot indicates that slightly superior to the central pupil is the area in which most of the cones are pointing. There are a total of 973 cones measured from Chick A

Figure 18: The 13 retinal images for chick B taken through the same varying entrance pupil locations as Chick A. A total of 1636 cones were measured from Chick B.

Figure 19: The retinal image of chick B, showing the deviation from the ensemble average for each individual cone.

Figure 20: The pupil intercept graph of chick B, measuring 1636 retinal cones' directionality.

List of Tables

Table 1: Reported distributions of the cone and rod photoreceptors in the chick retina [28]-[30]. The methods used to obtain the cone distribution are electron microscopy (E.M.) and the periodic acid-Schiff reaction (PAS). The variation seen between studies is due to both the measurement method and the location of the retina that was measured.

Table 2: The average cone directionality and angular tuning found by Roorda & Williams [42] in human subjects J.P. and G.Y. The rho values (ρ) indicate a narrow tuned function, in which the majority of cones are pointing in a similar direction toward the pupil. The X and Y peaks indicate which average direction the cones are pointing.

Table 3: (A) Operating parameters of the AO fundus camera at NECO during the imaging experiment. (B,C) Operating parameters of the deformable mirror (DM) and wavefront sensor (WFS) of the system.

Table 4: Physical and optical properties of chick A and B at the time of the experiment.

Table 5 The average cone directionalities and angular tuning for both chicks are given above. ρ and σ are related through the equation $\rho = 0.434/2\sigma^2$ *The x peak and y peak represent the average directionality of the cones.*

Table 6. Comparison of our findings in the chick eye to the human eye data from Roorda and Williams [42].

Introduction

The chick retina is a widely used animal model in the study of eye growth, in particular for the study of emmetropization and myopia. Like most vertebrate animals, the ability to image the fine retinal structure is degraded by the optical aberrations of the cornea and lens. The inability to visualize single cells in-vivo requires sacrificing the animal and preforming analyses on excised samples. Such samples are prone to preparation artifacts, such as drying and stretching. The capacity to monitor individual retinal cells has obvious applications in basic vision research and also in the diagnosis and treatment of a host of diseases.

In 2011 Headington et al.[1] provided the first *in vivo* images of the chick photoreceptors using the Adaptive Optics (AO) fundus camera at the New England College of Optometry (NECO). Six-week-old White leghorn chickens were imaged under general anesthesia, creating a montage of the collected 2.5° field of view (FOV) images. The fundus camera used was originally designed for imaging the human retina and a sub-system of lenses was used to de-magnify the 6 mm entrance pupil down to a 2 mm pupil in order to accommodate the chick eye [1]. Here we use the same AO fundus camera, slightly altering the lens sub-system to image over a 3mm rather than 2mm pupil. We utilize the unique high-resolution imaging capability of the system to look at a specific property of the cone photoreceptors, namely the Stiles-Crawford Effect of the First Kind (SCE-I) in the living eye.

Many studies have explored the changes in the photoreceptor alignment in diseases affecting the human retina [2]-[21]. In human eyes the spacing and orientation of photoreceptor cells is abnormal in refractive and disease processes. Changes in cone density with myopia have already been demonstrated in humans [14][19]. It has been found that in myopia, cone photoreceptor cells located nasal to the fovea orient toward the temporal optic disc, rather than toward the central pupil as is seen in emmetropia [14]. In retinal diseases such as central serous chorioretinopathy, in which the photoreceptor cells become disoriented, the measured optical SCE-I has proved a sensitive indicator of photoreceptor recovery [6]. Additionally, studies of directional sensitivity loss in patients with retinitis pigmentosa suggest that there is increased disarray of the cones in this disease [3][4]. In general, retinal diseases that exhibit outer retinal disruption are likely to show an alteration of the normal SCE-I.

Based on the work beginning in 1933 with Stiles and Crawford [22], it has been established that humans, and other species exhibit cone pointing, a phenomenon in which photoreceptor cells orient themselves toward the center of the pupil to achieve higher optical signal and be maximally efficient at capturing light - SCE-I [23]-[26]. Many retinal diseases exhibit a compromise in the SCE-I secondary to cone disruption. These conditions include myopia [14][19], amblyopia [18][20][21], central serous chorioretinopathy [6], retinitis pigmentosa [3][4], age-related-macular degeneration [5][7]-[9], trauma [10], fibrous scars [11], and gyrate atrophy [12]. Measuring the SCE-I in patients is a potentially quick and sensitive way to detect cone disturbance in diseased retinas [8]. The work presented here is the first to measure the cone directionality in the living chick eye by

directly imaging the photoreceptors, the goal being to present the chick eye as a viable animal model for the change in wave-guiding properties observed in human disease cases.

The following subsections discuss the properties and structure of the chick eye and describe the SCE-I in more detail before concluding with an introduction to the principle of AO.

STRUCTURE OF CHICK EYE AND PHOTORECEPTOR CELLS

The chick eye uses the same basic image forming optics as the human eye, consisting of a cornea, pupil aperture, and lens system to focus light onto the retina. The primary optical properties of the ocular tissues in the chick are shown in Figure 1.

(A) (B)

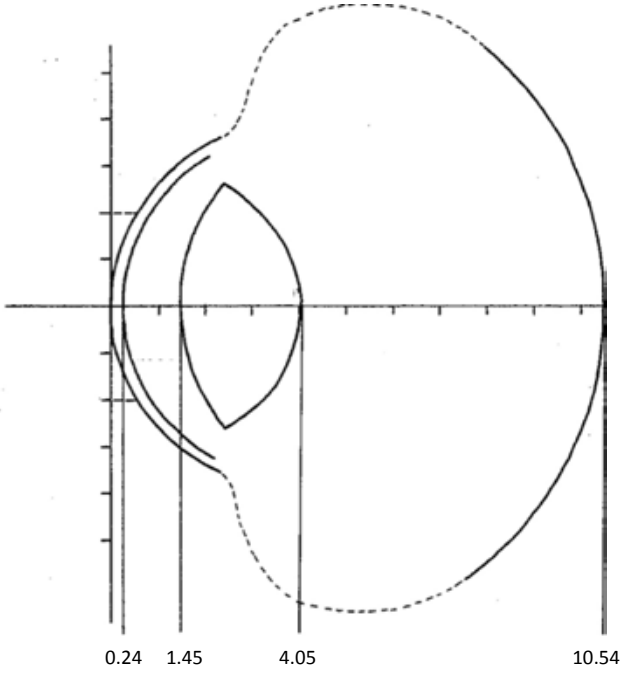

Optical Tissue	Refractive index
Cornea	1.373
Aqueous Humor	1.335
Lens	1.37-1.43
Homogenous lens model	1.455
Vitreous Humor	1.335

Optical Interface	Radius of Curvature
Anterior Cornea	3.84
Anterior Lens	4.00
Posterior Lens	-2.90
Front of Retina	-7.30

Focal length (mm)	8.5
Pupil Size (mm)	3.5
Optical power (D)	~115

Figure 1 (A) A schematic of a 30-day old chick eye [27]; the numbers directly below the schematic layout indicate the distance in mm from the anterior surface of the cornea. Corneal thickness = 0.24mm; anterior chamber depth = 1.21mm; lens thickness = 2.60mm; Vitreous humor depth = 6.49mm; axial length = 10.54mm. (B) The refractive indices and radii of curvature of the ocular media in the 30 D old chick eye [27]. The focal length of the 30D old chick eye is approx. 8.5mm and the dilated pupil diameter is about 3.5mm. The total optical power of the adult chick eye is ~115D.

The main differences between the chick and human retina are in the vascularity and photoreceptor cell topography. The mostly avascular chick retina receives oxygen and nutrients from the pecten (the only vascular area in the retina). Additionally, the distinct fovea area present in humans is not seen in the chick retina, although some studies have

found a central area with concentrated cones near the pecten [28]. Different cell topography studies have found varying distributions of cones and rods in the chick retina, and are compared in Table 1. In three of the four studies compared, electron microscopy was used to compare retinal sections of adult chickens [29][30]. The fourth study used the periodic acid-Schiff reaction and unfixed retinal mounts to differentiate between rods, cones and accessory cones in the adult chicken [28]. There are somewhat conflicting results among the studies, likely because they collected samples from different areas of the retina.

Investigator	Method	Retinal location	Cell distribution (%)		
			Single Cones	Double Cones	Rods
Morris and Shorey (1967) [29]	EM	Posterior pole	36.0	36.0	15.0
Morris (1970)[30]	EM	Posterior pole	54.0	32.0	14.0
Meyer and May (1973) [28]	PAS	Entire retina (other than HD area near pecten)	20.0	40.0	40.0
	PAS	High density area near pecten	23.0	45.0	32.0

Table 1: Reported distributions of the cone and rod photoreceptors in the chick retina [28]-[30]. The methods used to obtain the cone distribution are electron microscopy (EM) and the periodic acid-Schiff reaction (PAS). The variation seen between studies is due to both the measurement method and the location of the retina that was measured.

Avian cone photoreceptor cells, unlike those in the human retina, contain a wavelength sensitive 'oil droplet' in the ellipsoid of the cells, so named because of a high-lipid content [31]. These oil droplets contain carotenoid pigments, giving the cells a brightfield appearance and fluorescent properties when imaged [32]. Five different cone types have been described: four 'single' cones contain spectrally distinct oil droplets whose

sensitivities range from ultraviolet to 586nm, and a fifth 'double' cone that is sensitive to longer wavelengths [33][22] - Figure 2 and Figure 3. Double cones are the most prevalent (40.7%), notably ventrally, green are present in the next greatest abundance 21.1%, then red 17.1%, blue 12.6%, and violet 8.5% [32]. Oil droplets completely cover the entrance aperture of the outer segment, and ultimately represent the chick cone diameter, which is between 3.2 and 4.7μm in adults [15]. No oil droplets are found in rods, which are approximately 4μm wide, 40μm long and have a peak sensitivity at 506nm [15][16].

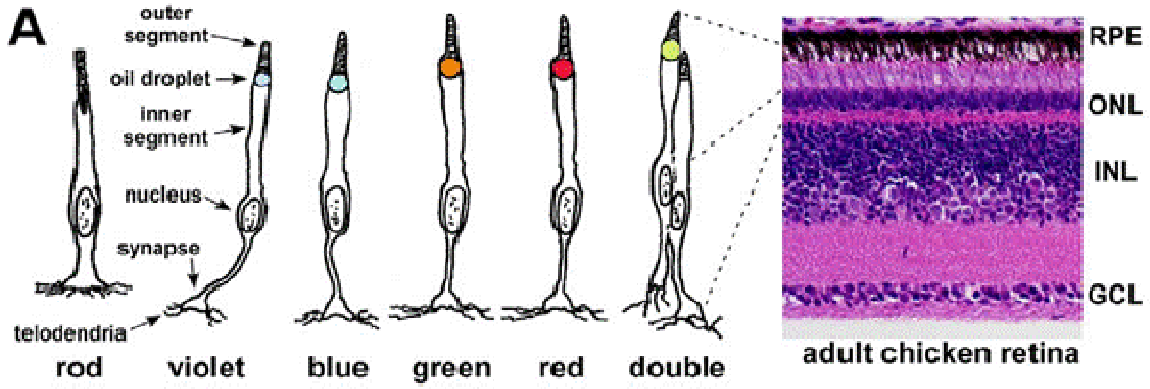

Figure 2: Chick photoreceptor cell schematic of rods and the 5 spectrally distinct cone types [32]. The oil droplet between the inner and outer segments is responsible for determining spectral sensitivity. The right side of the image shows a cross section of the adult chick retina, layers from posterior to anterior are retinal pigment epithelium (RPE), Outer nuclear layer (ONL), Inner nuclear layer (INL) and ganglion cell layer (GCL). The rod and cone cell bodies are located in the ONL.

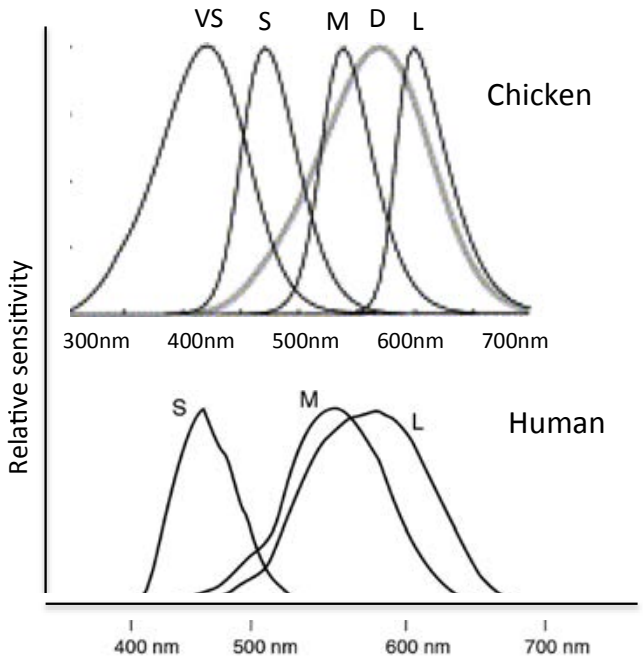

Figure 3. Spectral sensitivities of the various cone types in the chicken and human retina [34]. The top graph shows the spectral sensitivities of the 5 different chick cone types, whose sensitivities range from 300-700 nm (VS: very short; S: short; M: middle; D: double; L: long wavelength sensitive). The spectral sensitivities of the 3 distinct human cones are seen in the bottom graph (S: short; M: middle; and L: long wavelength sensitive), and range from 400-700nm.

THE STILES CRAWFORD EFFECT OF THE FIRST KIND (SCE-I)

When Stiles and Crawford first studied the effect of paraxial rays on the perceived brightness of light entering the eye, they found that light rays entering at the pupil edges were perceived as less bright, to a human observer, than the rays entering near the visual axis [22]. The phenomenon that the photoreceptors' response to paraxial rays is less than their response to centrally entering rays of equal intensity is termed the Stiles-Crawford Effect of the first kind (SCE-I).

Note this is distinct from the SCE of the Second Kind, a similar phenomenon in which the perception of color hue changes when a monochromatic light source enters the pupil at an oblique axis as compared to entering on the normal axis. By having patients color match 2 monochromatic lights of the same wavelength: one which traversed the pupil directly through the center, and the other of which traversed obliquely., Stiles found that patients perceived a different hue for the same monochromatic light. Ultimately, his experiments yielded interesting results: when yellow-orange light traversed the pupil at an oblique axis the hue shifts toward red; blue light perception shifts toward that of green light; interesting though, when green light entered the pupil obliquely, the hue perception shifted toward that of blue light. Stiles' ultimate conclusions found that at the level of the photoreceptor, long columns of highly concentrated pigment absorb normally incident light, while much thinner layers of pigment absorb obliquely incident light, narrowing the absorption spectra of the photoreceptor cell [35].

The SCE-I represents the ability of photoreceptor cells to behave as optical fibers [22][23][36]. The light energy that propagates down the cone does so in various

waveguided modal patterns, which are influenced by properties of the light and cell's physical characteristics [26],[37]-[39]. The physical properties that influence the SCE-I are as follows: configuration of receptor, diameter of receptor, index of refraction of the receptor and surrounding media, wavelength of energy introduced, and angle of incidence of light energy. The interactions among these physical properties together impact the observed waveguide patterns. Furthermore, the ellipsoid acts as an impedance-matching device in the cell, maximizing power transfer and minimizing reflections within the photoreceptor system [26].

Previous studies have explored the reflectance patterns of individual photoreceptor cells and their relationship to the directional movements that occur in order to orient cones toward the pupil center [40][41]. Various movements within the cone are involved in the directionality that is ultimately observed as the SCE-I. In the mid-twentieth century, researchers found that the outer segment lamellae, including the photopigment within the lamellae and the mitochondria in the ellipsoids, are spatially oriented and likely play a role in overall cell directionality [26].

PREVIOUS STUDY MEASURING CONE DIRECTIONALITY IN HUMANS USING AO

In 2002, Roorda and Williams [42] measured the cone directionality of two human subjects using an AO *in vivo* imaging system, and a 550nm krypton flashlamp to illuminate the retina at various entrance pupil locations. The images were collected at a location 1 degree nasal to the fovea, representing seven entrance pupil locations: one central entrance location and six surrounding locations (circular around the center). They measured scattered light from each imaged cone as the angle of illumination was changed, and ultimately determined the acceptance angle of the cone. This method is an accurate way to measure cone directionality because it is known that the amount of light scattered is related to the amount absorbed by the cone. In using this method (rather than measuring angular tuning directly), they also reduced the effect that the coherence of the cones would have on the angular tuning measurement.

In their study, Roorda and Williams [42] measured the average reflected intensity of each individual cone in each of the seven entrance pupil images. The average intensities of each cone (7 measurements) were then fitted to a Gaussian function in order to determine the pointing in the pupil plane of the eye. The average cone directionality and angular tuning values from this experiment are shown in Table 2. Collecting data from a total of 200 and 275 cones in two subjects, they found that cones point with little disarray, and those in close proximity to each other are more likely to be arranged in the same (random) direction. The rho (ρ) values indicate a narrowly tuned Gaussian function, in which most of the cones are pointing in a similar direction toward the pupil.

Subject	Average cone directionality (entrance pupil position)		Average angular tuning	
	X peak (mm)	Y peak (mm)	σ	ρ
J.P.	1.41	0.194	1.50 +/- 0.07	0.096
G.Y.	0.11	0.19	1.66 +/- 0.05	0.079

Table 2. The average cone directionality and angular tuning found by Roorda and Williams[42] in human subjects J.P. and G.Y. The rho values (ρ) indicate a narrow tuned function, in which the majority of cones are pointing in a similar direction toward the pupil. The X and Y peaks indicate which average direction the cones are pointing.

MEASUREMENT OF THE SCE-I IN THE LIVING CHICK EYE USING ERG RECORDING

In 1999, Beresford et al. [43] established a technique for measuring SCE-I in 3-week-old chickens using LED stimulation and recording electro-retinograms (ERG). They stimulated the central 22.5 degrees of the subjects' retina using several LED arranged 7.5 degrees apart in an 150mm arc. These LEDs, located at the entrance pupil of the imaging system, illuminated simultaneously through a pinhole/lens system and onto the chick's retina. The peaks of the a and b-wave recordings from the ERG were then fit to Gaussian functions in order to plot the Stiles-Crawford effects of the photoreceptor cells. Based on the "peakedness" of the ERG recordings (height of the a and b waves), they determined the directionality of the cone, finding that central retinal cells orient slightly superior to the central pupil, and inferior and superior cells orient toward the center of the pupil (inferior cells with slightly more accuracy than superior cells). Further, they found there to be a .215-.221 total topographical change among photoreceptors across the central retina [43], or simply the percentage change in cone directionality across the central 22.5 degrees of the retina.

THE NEED FOR ADAPTIVE OPTICS

All optical systems have a limit to their resolution based on diffraction. The theoretical limit to the resolution of an optical system with a circular pupil is given by:

$$r = (1.22 f \quad) / D \qquad (1)$$

where r is the radius of the focused spot, f is the focal length of the eye, is the wavelength of the light used for imaging, and D is the pupil aperture size. In a biological system like the eye, the soft tissues act as optical elements and have aberrations by nature, which further limit their resolution capabilities. Based on diffraction (D=7mm, f=17mm, =550nm), the human eye should have a lateral resolution of 2-3um; however, aberrations within the optics limit the actual resolution to about 10μm [44].

Figure 4 shows the wavefront and PSF profiles for a circular pupil and a typical human eye (with zeroed second order aberration coefficients) for a 6 mm diameter pupil in 650 nm imaging light measured with the NECO AO system. Zero aberration gives the well-known Airy disk diffraction pattern. The typical human eye, particularly when dilated, suffers from considerable aberrations, which reduce the Strehl Ratio (SR) to around 0.11. The low SR results in poor retinal images with low contrast. A perfect, un-aberrated image has a SR of 1 with anything over 0.8 is said to be diffraction limited.

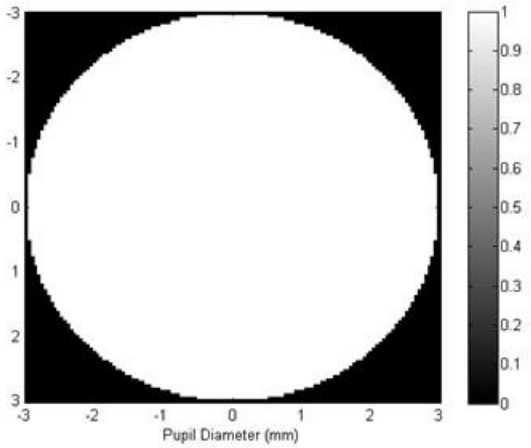

(A) – *Wavefront plot for a circular pupil with no aberration*

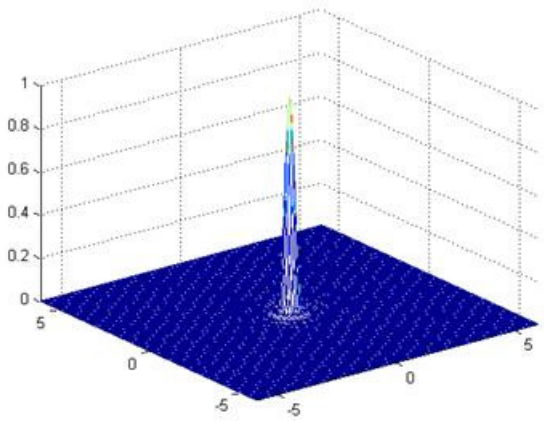

(B) – *Un-aberrated PSF. Strehl Ratio = 1. Perfect Imaging*

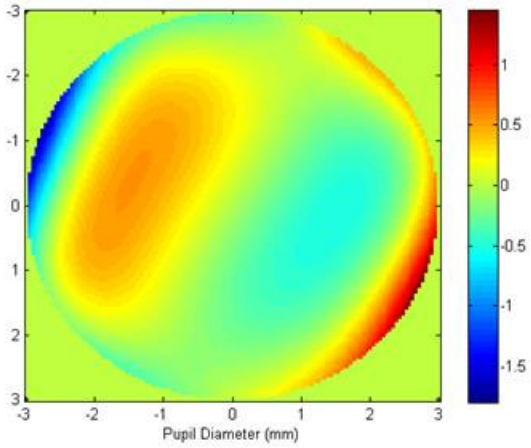

(C) Wavefront plot for a typical human eye with zeroed second order coefficients. RMS error = 0.36 µm, PV error = 2.8 µm.

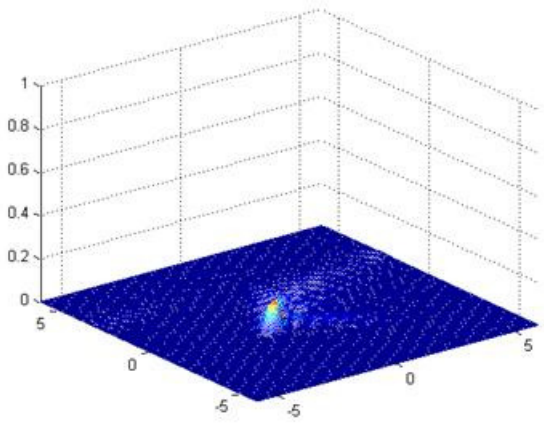

(D) PSF plot for a typical human eye with zeroed second order coefficients. SR = 0.11

Figure 4: Effect of aberrations on the wavefront profile and far field point spread function (PSF) (A) The un-aberrated case gives a flat wavefront and the characteristic Airy disk pattern PSF (B) (C) Typical profile for a normal human eye. A SR > 0.80 is said to be diffraction limited. 6 mm pupil diameter, 650 nm measurement wavelength.

Adaptive Optics (AO) was first employed by the US military in the 1970s to ameliorate the effects of the Earth's atmosphere when imaging from terrestrial telescopes. The 1980s saw the declassification of the technology and the rapid uptake from the astronomy community. The late 90s saw the first use of a wavefront sensor (WFS) and then the use WFS in conjunction with a deformable mirror (DM) to give the first AO system for the eye [45].

The use of AO has spread to ocular imaging devices, which can create high-resolution images of the retina through an aberrated cornea, lens and vitreous. In the vertebrate eye, the resolution of an image at the retina is less than the calculated resolution based on diffraction. In a diffraction-limited system, as the diameter of an aperture increases, the resolution of a system increases. However, in the human, chicks and other vertebrates, a large pupil introduces higher magnitude aberrations from the optical media. An AO system allows imaging through a large pupil because it corrects the aberrations brought on by the ocular media. Figure 5 outlines the principle of an adaptive optics system used to image the retina. In the system, both the DM and the WFS receive incoming, aberrated light reflected off the retina. The WFS senses the aberrations and signals the DM to adjust the mirrors to a conjugate wavefront formation, which correct the aberrated wavefronts coming from the retina. This cycle ultimately allows the formation of an un-aberrated retinal image on the camera. Furthermore, the system runs in a real time loop, the DM pistons adjusting dynamically as they receive continuous input from the WFS. In these imaging systems, the resolution of retinal images becomes limited by diffraction only.

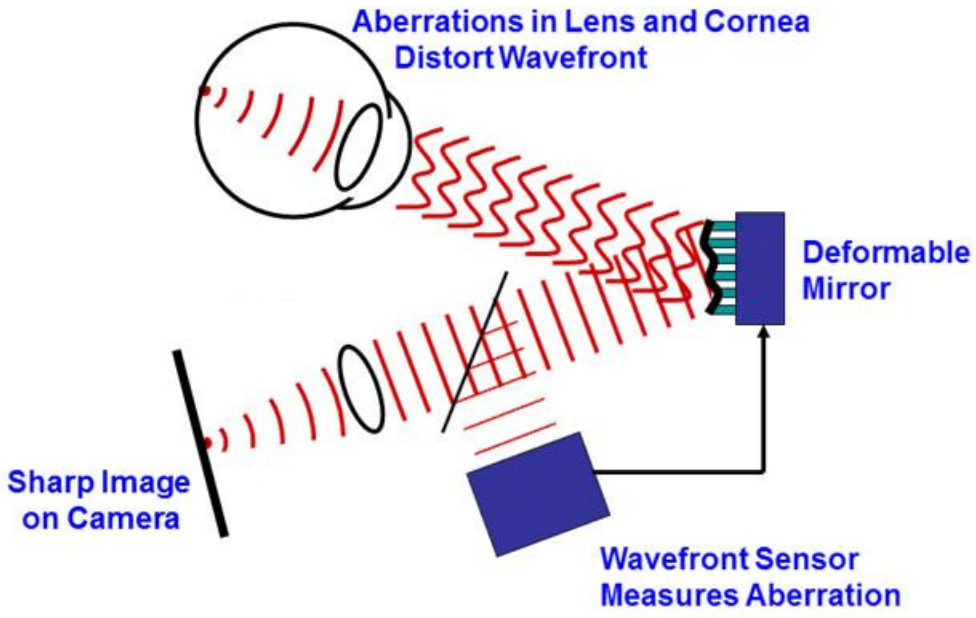

Figure 5 The principle of AO. The deformable mirror receives incoming aberrated light reflected off of the retina. This light is also captured by the WFS, which senses the aberrations and signals the DM to adjust the mirrors to a conjugate wavefront formation. The aberrated light from the retina is then corrected during reflection off the DM and continues on to form a clear, un-aberrated image on the camera. Furthermore, the system runs on a real time loop, the pistons adjusting dynamically as they receive continuous input from the wavefront sensor.

An AO system comprises three main components:

i) **The Wavefront Sensor (WFS)** – this measures the optical aberrations in the incoming distorted wavefront. The most common form is vision science is the Hartmann-Shack WFS and its principle of operation is shown in Figure 6.

ii) **The Control Computer** - this takes the output of the WFS and converts it to voltage commands that are sent to the wavefront corrector.

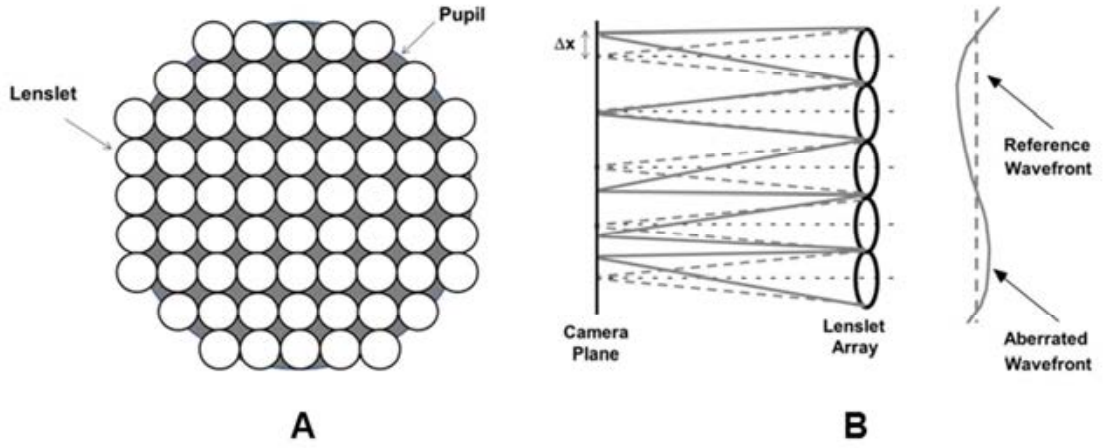

Figure 6 Principle of the Hartmann-Shack WFS. (A) the incident pupil shown with the gray circle is sampled by a two dimensional array of lenslets. (B) Cross section through the (A). For the reference wavefront shown by the gray hatched line a focal spot is formed by each lenslet on the camera plane and is exactly centered behind each lenslet. For an aberrated wavefront (solid gray line) variations in the slope between each lenslet will cause the focal spots to be shifted from the position of the reference. By determining both the Δx and Δy shifts for each lenslet the aberrated wavefront may be reconstructed. It is important that the WFS samples the incident wavefront with sufficient speed (20-30Hz) to accurately track any temporal changes.

iii) **The Wavefront Corrector** - this device provides the conjugate correction to the measured optical distortions. The aim of any wavefront corrector is to equalize the optical path length (OPL) seen by all points on the incident wavefront, resulting in a flat wavefront after correction. Deformable mirrors (DMs) are by far the most common devices used. These operate by locally deforming a mirrored surface i.e. they change the physical path length. Figure 7 shows cross sections through the three broad categories of DM. The particular DM used in this study was the segmented piston/tip/tilt design – Figure 7C.

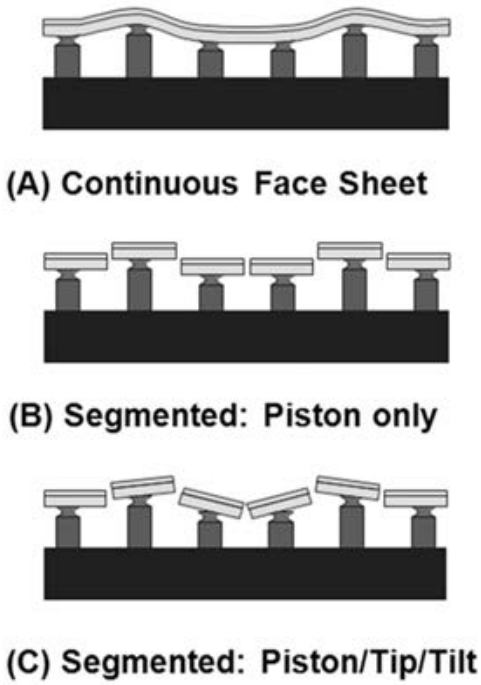

Figure 7 Deformable mirror types. (A) Continuous face sheet – a continuous mirror surface is deformed by an underlying array of actuators. (B) The mirror surface is composed of a discrete array of segments each of which may move in a pure piston (vertical) motion only. (C) Similar to (B) but each segment may now also move in tip and tilt in addition to piston. This is the type of DM employed for the work described here.

The actual DM used in these experiments is shown in Figure 8. The overall mirror surface is comprised of a series of segments each of which has independent piston/tip/tilt control. Manipulating all segments allows for the generation of arbitrary wavefront profiles.

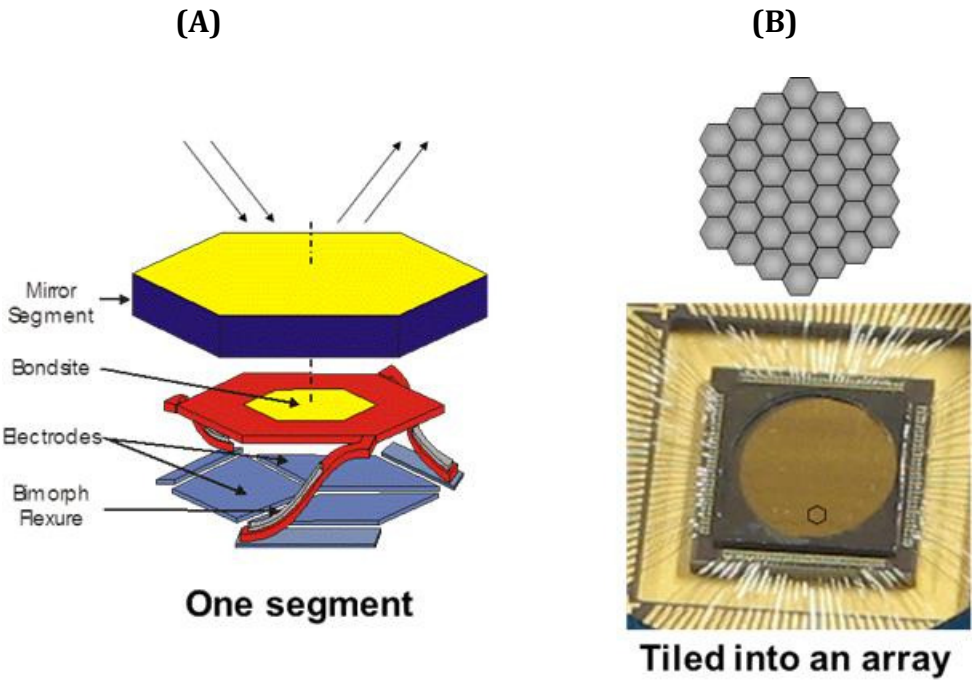

Figure 8 (A) One of the DM segments, which is bound to a piston-like platform that allows for axial as well as tip/tilt movements. (B) The 37 mirror segments are arranged into an array to form the overall DM surface.

The specific properties of the WFS and DM used for the NECO AO fundus camera are described in detail by Headington et.al. [1]. The optical layout of the AO fundus camera, including the modifications made for the chick imaging, are displayed in Figure 9.

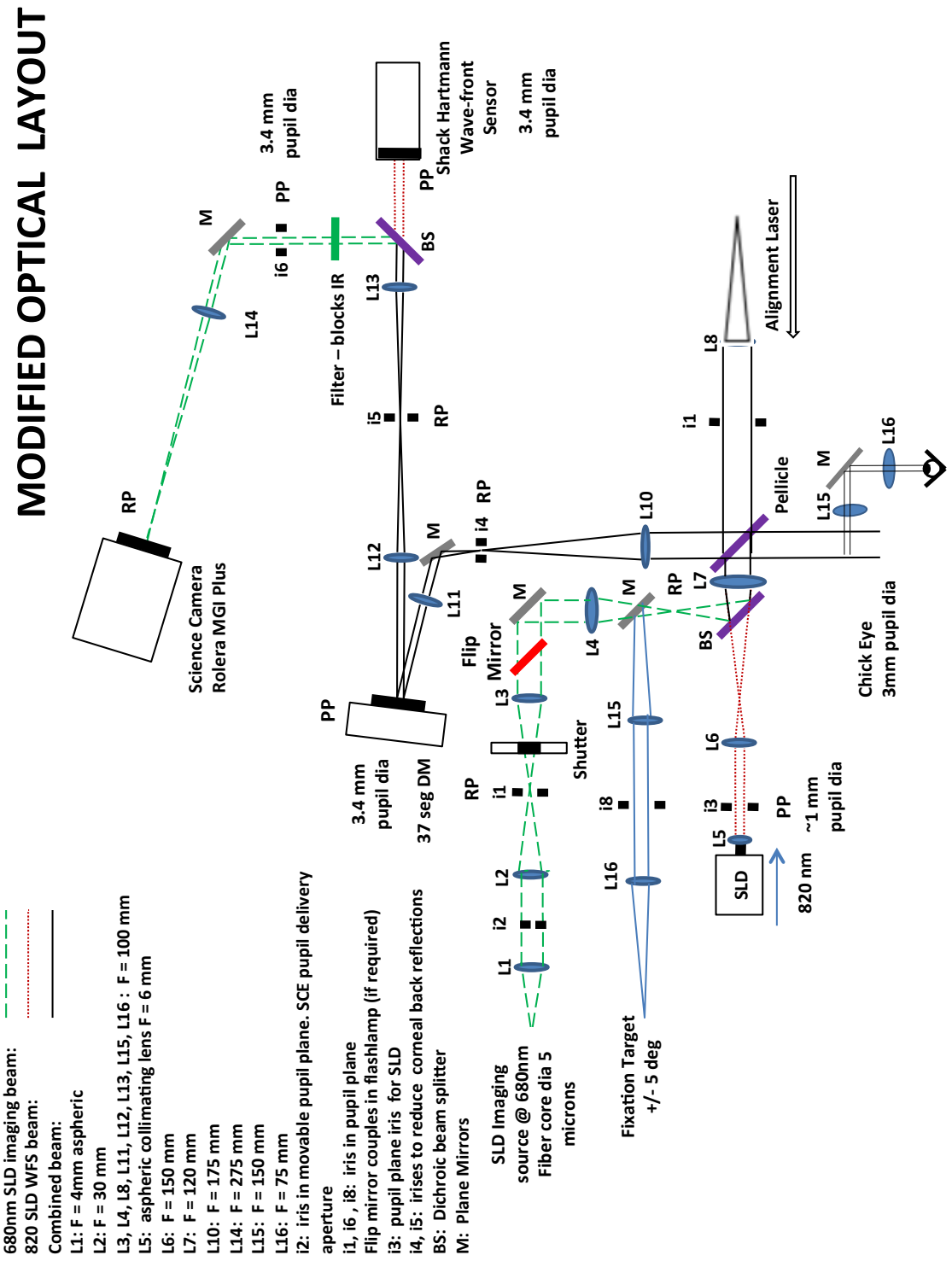

Figure 9 The original optical layout of the AO Fundus Camera at The New England College of Optometry, with the added lens modifications for imaging chick eyes. The modifications made to the system are lenses 15 and 16 along with the mirror that reflects the light downward.

In 2012, the laboratory established a protocol for imaging chick photoreceptor cells with the AO fundus camera at the New England College of Optometry [1]. Figure 10 is an image from the retina of chick B, taken using the AO system. NECO's AO fundus camera has lateral resolution capabilities of approximately 2.5um for a 6-week-old chick, sufficient for our cone imaging study [1].

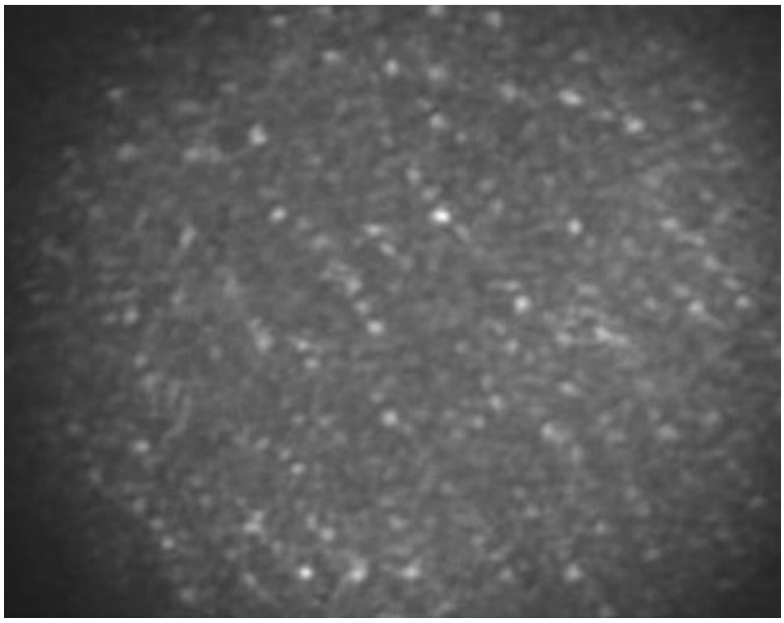

Figure 10 A 1° FOV fundus image of chick B, taken using the AO fundus camera at NECO (imaging beam 650nm). The image is a registered sum of 4 raw images. The illuminated areas represent reflections from cone cells in a live 48-day old White Leghorn chicken.

Using AO, we extend this imaging capability and demonstrate for the first time, a direct measure of cone directionality using retinal imaging in the living chick eye. The next section introduces the methods we employed to determine the cone pointing in the retinas of adult chickens.

Methods

ANIMALS

The animals used in this study were cared for in accordance with the National Institute of Health Guide for Care and Use of Laboratory Animals and the NECO Institutional Animal Care and Use Committee (IACUC). Two white leghorn chickens (*gallus gallus domesticus*) were hatched and housed in NECO's animal facility and are labeled for this work as chick A and chick B. Their housing units were temperature regulated and under a 12-hour light/dark cycle (light from 8:30am-8:30pm). Food and water were provided ad libitum.

The birds were used for imaging at approximately 48 days old, weighing an average of 585g. The day of the imaging procedure, refractive and ultrasound measurements were taken. Prior to anesthesia, birds were dilated using vecuronium bromide, applied every 5 minutes for 30 minutes. Fully dilated pupils ranged from 3.2-3.6 mm in diameter. Anesthesia was administered through an intramuscular injection with a mixture containing 1mg/kg ketamine and 0.2mg/kg xylazine. Immediately following the anesthetic injection, the bird was mounted onto the imaging stage (Figure 11) and secured using an insulated blanket and tape. The beaks of the chicks were secured to a bite bar to ensure precise alignment of the eye, and the eye was held open using a lid speculum. As needed, non-preserved Celluvisc (Allergan) artificial teardrops were instilled to maintain corneal hydration; since the nicotinic membrane of the chick continues to function under anesthesia, frequent hydration was not necessary. In order to maximize available time, the AO imaging began immediately after the anesthetic injection, with a session typically

lasting 45 minutes to an hour. Deep anesthesia was maintained during experimentation with a half-dose of the anesthesia cocktail applied if required.

CHICK MOUNTING STAGE

The stage for chick imaging was specifically designed to secure the chick eye and allow precise alignment of the bird to the imaging system –Figure 11. It is critical that the pupil is centered on the optical axis of the system and is axially conjugate to focal length of the last lens. The main platform allowed for gross translation in XYZ directions. Directly beneath the platform was a goniometer mount, further allowing for the fine tip and tilt adjustments that were necessary precise alignment.

The chick beak was attached to mount to maintain head alignment. Once the beak was attached, the stage could be mounted below the AO system housing. The eye was then grossly translated upward until the corneal surface was 75 mm from the last lens of the AO system (i.e. the focal length of the last lens and the conjugate pupil plane).

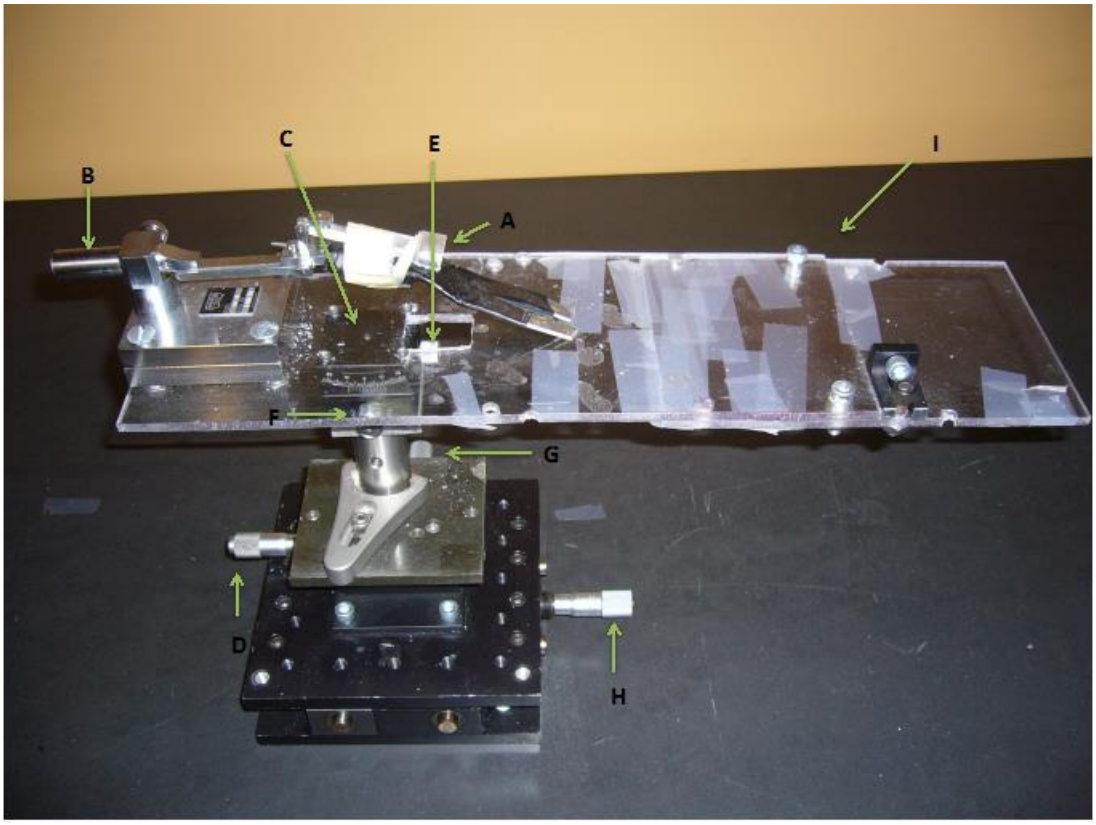

Figure 11 The stage used during the imaging procedure. (A) Bite bar used to position the beak of the bird. (B) rotation control for the bite bar (C) goniometer translation stage (D) vertical translation stage control knob. (E) control for fine rotation about the x-axis (F) control for fine rotation about the y-axis. (G) x-axis gross translation control (H) y-axis gross translation control. (I) platform used to hold the body of the bird.

AO SYSTEM MODIFICATIONS

The AO system at NECO was originally designed to image a 6mm human pupil. It was modified for imaging through a smaller chick pupil by adding a telescope with a 150/75mm focal length combination in order to de-magnify the 6mm pupil by a factor of 2. A mirror was placed between the two lenses of this additional telescope system in order to redirect the light beams downward, allowing us to image the animal in a supine position.

The AO fundus camera operates by projecting two beams into the eye. The super luminescent diode (SLD 820 ± 20nm) projects from the retina to the WFS (30Hz), which activates the DM to form a conjugate aberration profile. This conjugate waveform counteracts the aberrations in the eye, which would otherwise degrade the retinal image. The second beam is the imaging beam (650nm) that images the retinal plane, projecting to a conjugate plane: the imaging camera. A schematic of the AO system with the modified chick attachment is displayed in Figure 9, and the operating parameters of the system are outlined in Table 3.

A. OPERATING PARAMETER	VALUE
Pupil diameter	3 mm
Power of IR beam	10 µW
WFS beam diameter	0.75 mm
Imaging beam source	Mercury Xenon 600W arclamp
Imaging wavelength	650 ± 30 nm
Power of imaging beam	40 µW
Diameter of imaging beam	0.8 mm
Imaging camera type	Rolera MGI Plus
Imaging exposure time	10 ms
Field of view	1°

B. DM PARAMETERS	VALUE
Manufacturer	Iris AO Inc
Type	MEMS segmented piston/tip/tilt
Segment density	7x7 hexagonal packing
Mirror pitch (center to center)	606 µm
Mirror stroke	5 µm
Inscribed diameter	3.5 mm
Refresh rate	2.3 kHz
Voltage	110 volts
Fill factor	1:1
WFS: DM mapping	1:1
C. WFS PARAMETERS	VALUE
Manufacturer	Uniqvision UP-680-CL
Type	Shack-Hartmann
Lenslet density	7x7 hexagonal packing
Lenslet pitch	0.6 mm
Lenslet focal length	19 mm
Zernicke Reconstruction	Up to 5th order
WFS source	SLD 820 ± 20 nm
Sampling frequency	20 Hz

Table 3. (A) Operating parameters of the AO fundus camera at NECO during the imaging experiment. (B,C) Operating parameters of the deformable mirror (DM) and wavefront sensor (WFS) of the system.

CONE DIRECTIONALITY IMAGING

The procedure for measuring the cone directionality begins with imaging the retina through various entrance pupil locations. The chicks were mounted on a translational stage that allowed us move the eye in an x and y axis in 0.5 mm increments. By translating the chicken eye rather than the beam itself, we avoided inducing additional reflections into the aligned AO system. Figure 12 demonstrates the basic principle of imaging: the 650 nm imaging beam passes through an initial aperture and enters the chick eye. The chick eye was translated laterally using the mount in order to change the location of the beam on the corneal surface. Images were acquired at 12 locations surrounding the central pupil location – Figure 13.

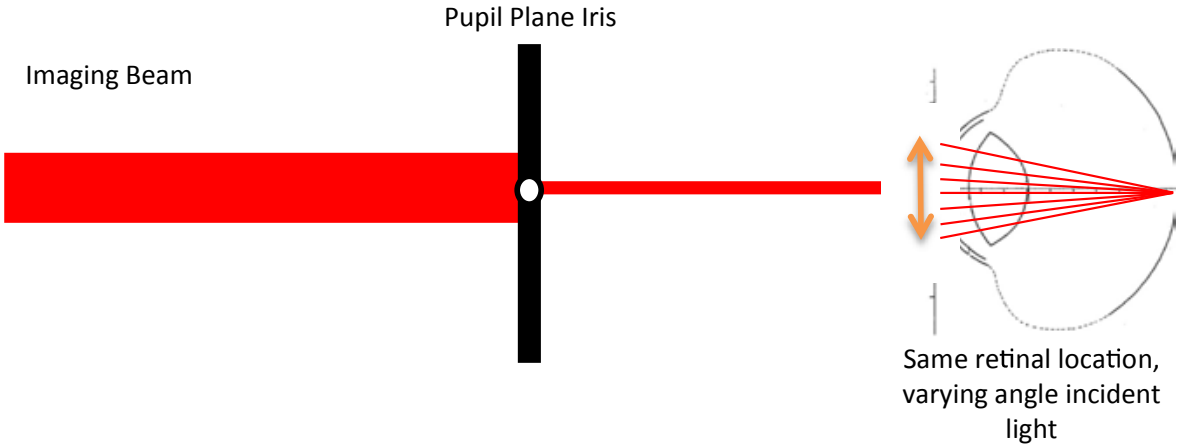

Figure 12 The chick eye was translated on the x and y axes in order to change the location of the entrance beam and create an oblique entrance angle. The same retinal cones were imaged at each entrance pupil position.

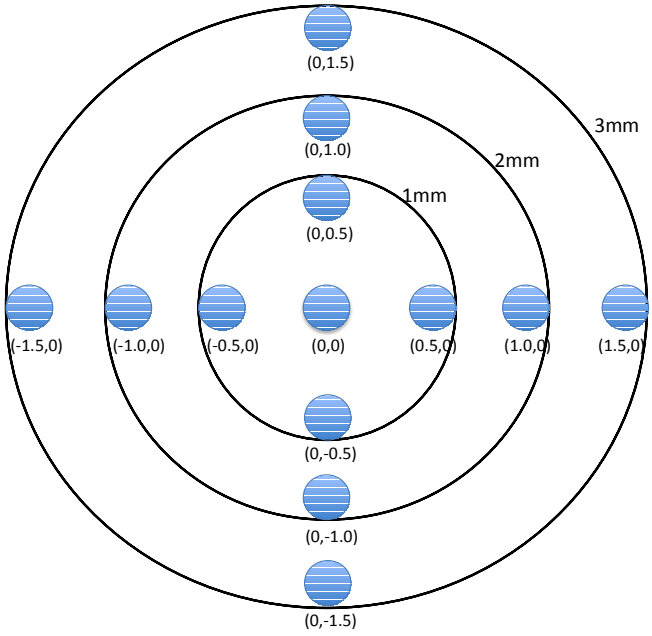

Figure 13 A diagram of the entrance pupil locations used during the imaging procedure. By translating and rotating the bird eye, we imaged the retinal cones through 13 different entrance pupil locations. There were 14 total batches of image collection (13 unique + 1 additional central point) through the 3 mm chick pupil. Each point on the figure represents the amount of translation in the pupil plane for each entrance beam location.

Prior to imaging, the AO system was calibrated to the specific requirements of the study. A light meter was used to measure the power of the SLD imaging and WFS beams incident at the pupil plane. System apertures were adjusted to increase or decrease the power of each source. The power of the WFS infrared beam was approx. 10 μW, and the imaging beam was set between 30 and 40 μW. Test images were captured using a model chick eye, and lenses and mirrors were adjusted to reduce light reflections from the various elements of the system.

In order to reduce image-degrading reflections in the system, we made all attempts to reposition the bird eye itself when necessary during imaging, rather than the entering

imaging beam, in order to avoid inducing reflections after the system was calibrated, as well as to maintain alignment between the imaging and WFS beams.

Once the bird was secured onto the stage and within the AO system, the DM centroids were brought up on a computer screen so that each centroid could be visualized. The pupil of the bird and (to a lesser extent) the lenses were adjusted in order to allow for full visibility of all centroiding spots. When the RMS value fell below 100 nm, the camera shutter opened for 10 msec and the imaging beam reflected off the dichroic beamsplitter and into the eye. Reflecting off the retina and back through the system, the light waves formed an image on the camera conjugate to the retinal plane. At each capture cycle, 20 frames (each with a 10 msec exposure) were collected. After 20 acceptable frames were collected for a single pupil position, the translational stage attached to the beak was moved to begin the measurement protocol. The translational stage was initially positioned at coordinates (0,0), and moved to the coordinates outlined in Figure 13. A 1-degree FOV was imaged at each location.

POST-PROCESSING USING MATLAB

The initial process was to sort through the acquired images and determine those with the highest quality. Matlab code written specifically for the experiment was used to analyze the data and determine cone directionality. Ultimately, 4 images for each entrance beam location were manually selected and registered together using Matlab to form one high quality registered image. Next, a total of 14 registered images (one for each entrance beam position plus an additional central position) were further registered together to form one final image for each eye; this step allowed us to confirm that we were imaging the same cones at each entrance pupil location. The images were then analyzed in another Matlab script designed for SCE-I measurements. The program selects cones, each which display a minimum pixel intensity (>1500 gray levels). The minimum distance between intensity points was selected as 5 pixels, in order to avoid double counting of a single cone. The intensities at the cone locations of the 14 registered images were averaged, and an average intensity for each location was determined. The Matlab program outputs the average horizontal and vertical pointing directions at the pupil plane, as well as the average angular tuning, sigma. These values were then fit to the Gaussian angular tuning function - equation 2 to determine the intensity at the pupil plane.

$$I_{pupilplane} = A \cdot \exp\{-((x - x_o) + (y - y_o)/2\sigma)\} \quad (2)$$

Where A = the peak reflectance, x_o and y_o are the pointing directions in the horizontal and vertical pupil planes, and sigma σ is the angular tuning spread.

Results and Analysis

Both subjects in this experiment were just under 7 weeks old (48 days) and weighed an average of 585g. Their dilated pupil diameters were between 3.2 and 3.6mm. Table 4 outlines the physical and optical properties of the chicks during the experiment.

	Chick A	Chick B
Age (days)	48	48
Weight (g)	600	570
Pupil diameter (mm)	3.6	3.2
Corneal refractive power (D)	39.33	41.42
Anterior chamber thickness (mm)	1.74	1.55
Lens thickness (mm)	2.70	2.89
Vitreous chamber thickness (mm)	7.79	7.05
Sensory retina thickness (mm)	0.21	0.22
Axial length (mm)	12.44	11.71
Focal length (mm)	8.55	8.05
Lateral resolution (μm)	2.74	2.90

Table 4 Physical and optical properties of chick A and B at the time of the experiment.

Effect of the AO Correction

The imaging sessions lasted between 45 minutes and 1 hour, maintaining general anesthesia throughout. Due to the sensitivity of the imaging system and the precision necessary to image such fine detail, it was important to maintain deep anesthesia throughout imaging. Under the anesthesia the chicks had paralyzed accommodation, but

micro-fluctuations remained which made it beneficial to correct the aberrations in real time. Our results prove good fixation due to all the retinal images being in register.

It is important to avoid blur as much as possible, not only to obtain clear images, but specifically to obtain accurate pointing data. We corrected for most lower order aberrations using trial lenses, but the remaining higher-order aberrations needed to be eliminated using AO – Figure 5. Any remaining blur in our experiment was caused by diffraction, uncorrected aberrations and a small amount of scattered light. Figure 14 shows the wavefront aberration and the associated point-spread function (PSF) before and after AO correction for chick B. The RMS error of the image before AO correction was 0.96 μm with an associated PV error of 4.4 μm and Strehl ratio (SR) of 0.02. After correction with AO, the RMS error decreased to 0.06 μm with a PV error of 0.41 μm and Strehl ratio (SR) of 0.70, demonstrating a large decrease in pupil plane aberrations after correction with AO. A larger SR (closer to 1) indicates a less aberration and hence improved imaging.

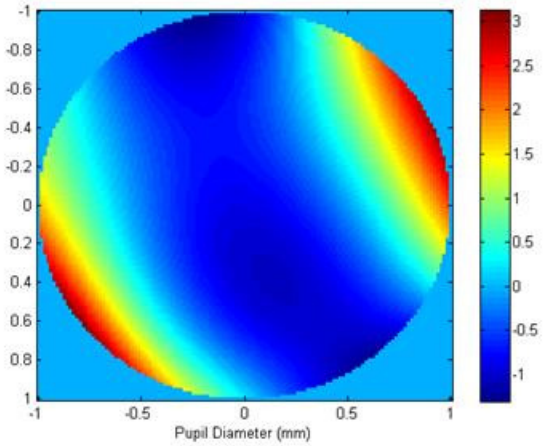

(A) – Wavefront plot AO 0ff. RMS error = 0.96 µm, PV error = 4.4 µm.

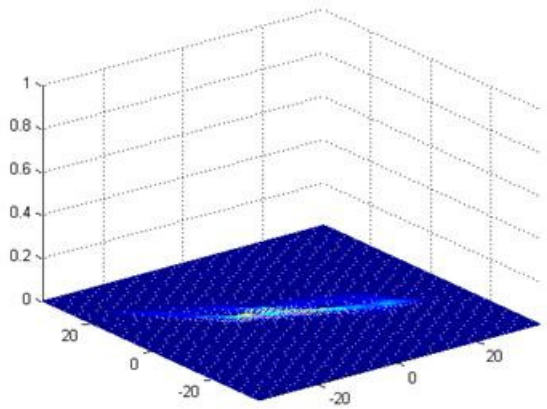

(B) – PSF plot AO off. SR = 0.02

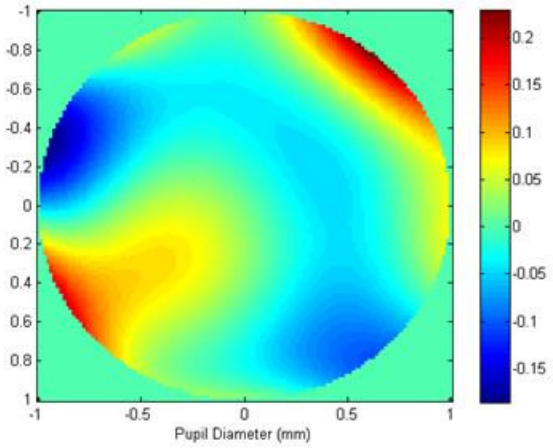

(C) Wavefront plot AO 0n. RMS error = 0.06 µm, PV error = 0.41 µm.

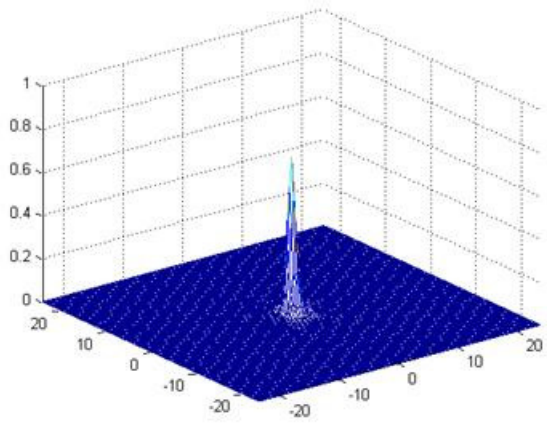

(D) PSF plot AO on. SR = 0.70

Figure 14 Before and after AO wavefront and PSF plots for chick B. The improvement in optical quality after correction (B and D) sets the condition for the high resolution imaging of the retina. The RMS error before AO correction was 0.96um with a PV error of 4.4um and Strehl ratio (SR) of 0.02. After correction with AO, the RMS error decreased to 0.06um with a PV error of 0.41um and Strehl ratio (SR) of 0.70.

Both blur and noise in an image not only degrade the image quality, but also affect the cone directionality measurements. Blurring causes noise from neighboring cones and underestimates the amount of measured cone disarray. Excess noise has the opposite effect on the cone directionality measurements, overestimating the amount of disarray [42]. By including a dark subtraction step in the processing of our raw images we were able to decrease the amount of noise.

Cone Directionality Results

The retinal images taken from chick A at the 13 different pupil locations are shown in Figure 15 with each image being the sum of 4 registered images. The numbers in parenthesis represent the axis position of the entrance position of the imaging light. Based on the positioning of the bird, the entrance pupil positions were superior, inferior, nasal, or temporal on the bird as shown by the key. The luminance change seen in the images as the entrance beam moves away from the central pupil represents the decreased cone response to light rays entering the pupil at oblique axes.

The angular tuning properties of each individual cone could then be fitted using the Gaussian function that was outlined in Equation 2. The location of the peak of the Gaussian function from the pupil center (taken to be the origin) gives the angle and magnitude of the cone pointing. Figure 16 displays the retinal image for chick A, showing the deviation in pointing from the ensemble average for each individual cone. The red circle represents the cone center with the direction and length of the line showing the angle and magnitude respectively. The data can be re-plotted in the pupil plane by using the location of the Gaussian peak as the pupil intercept – Figure 17.

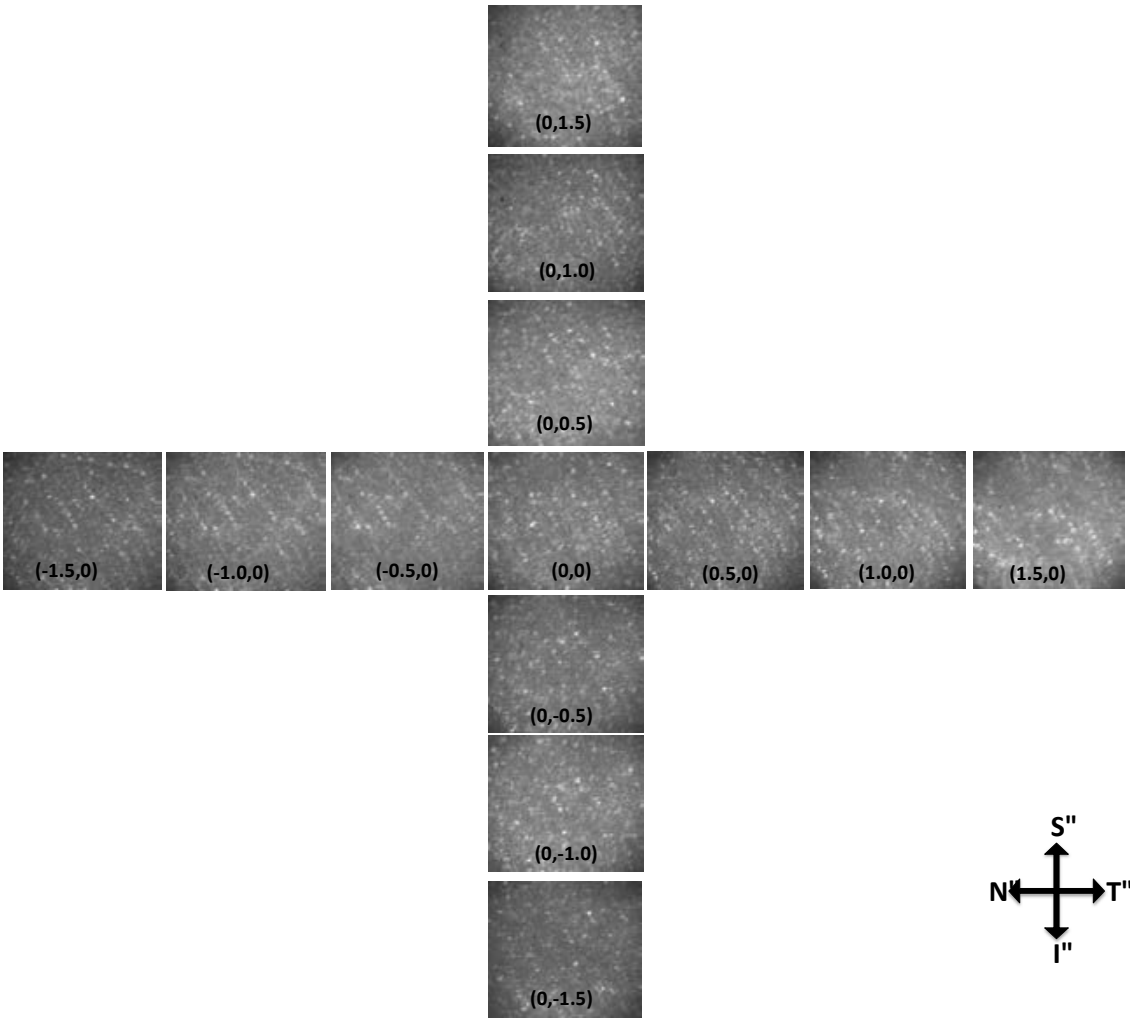

Figure 15 The retinal images taken from chick A at 13 different pupil locations. Each image is the sum of 4 registered images. The numbers in parenthesis represent the axis position of the translation stage relating to the entrance position of the imaging light. Based on the positioning of the bird, the entrance pupil positions were superior, inferior, nasal, or temporal on the bird as shown by the key. The intensity changes that are seen as the entrance beam moves away from the central pupil represents the decreased cone response to light rays entering the pupil at oblique axes. The intensities for each plot have been normalized to illustrate the change in brightness of the image as the entrance pupil position moves away from the peak coupling.

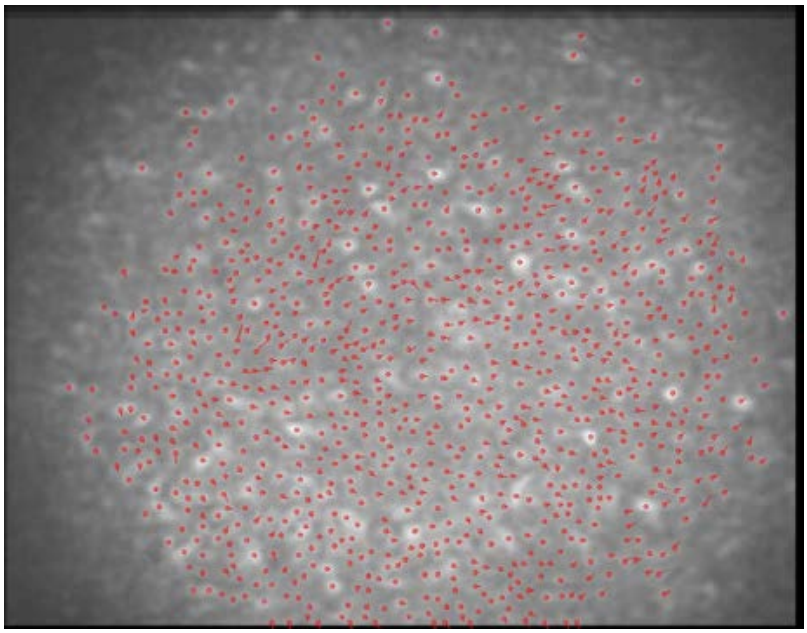

Figure 16. The retinal image of chick A, showing the deviation from the ensemble average for each individual cone. The red circle represents the cone center with the direction and length of the line showing the angle and magnitude respectively.

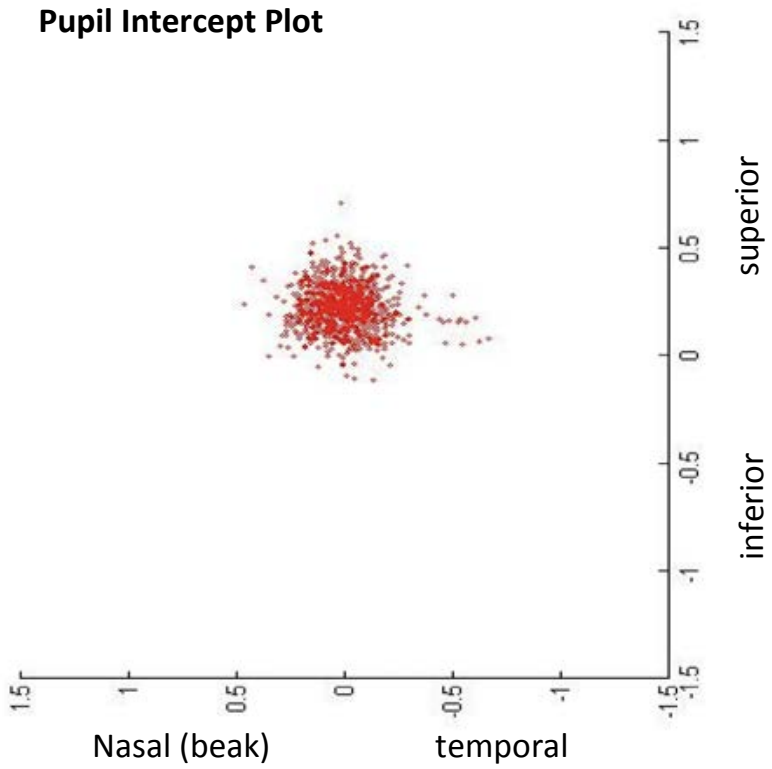

Figure 17. The pupil intercept graph of chick A, which show a fairly narrow distribution of pupil locations, indicate the points of the pupil that each cone would reflect light through based on their directional positioning. This plot indicates that slightly superior to the central pupil is the area in which most of the cones are pointing. There are a total of 973 cones measured from chick A

The equivalent plots for chick B are shown in Figure 18, Figure 19, and Figure 20.

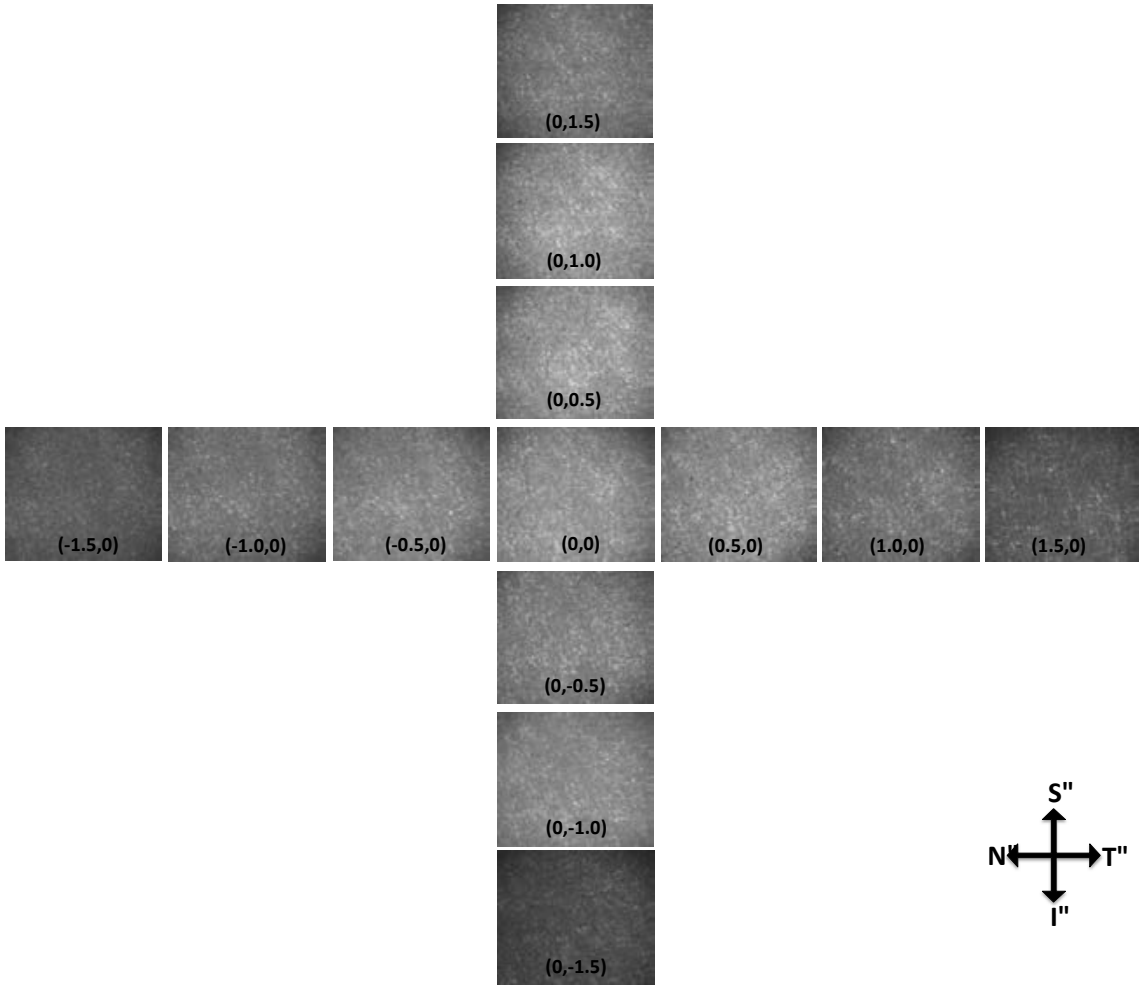

Figure 18. ***The 13 retinal images for chick B taken through the same varying entrance pupil locations as chick A. A total of 1636 cones were measured from chick B.***

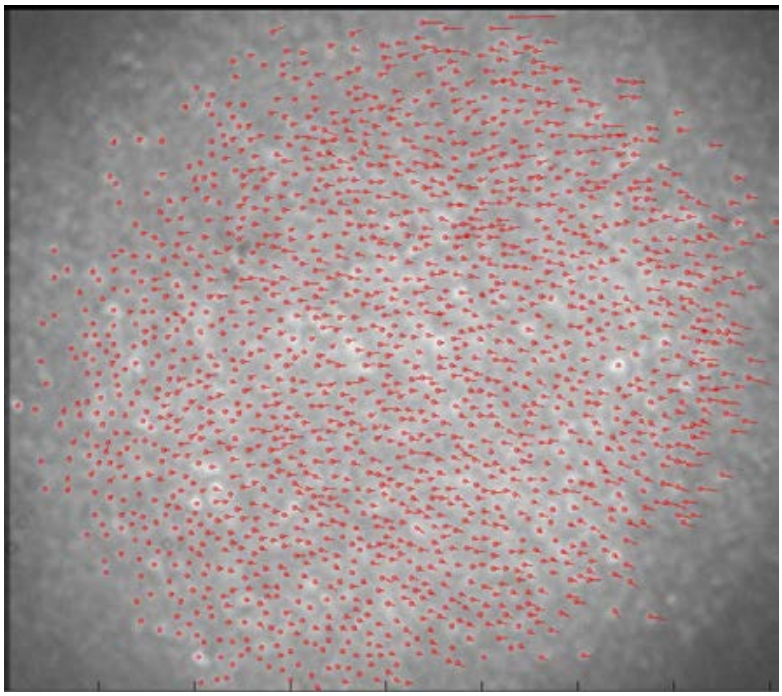

Figure 19. The retinal image of chick B, showing the deviation from the ensemble average for each individual cone.

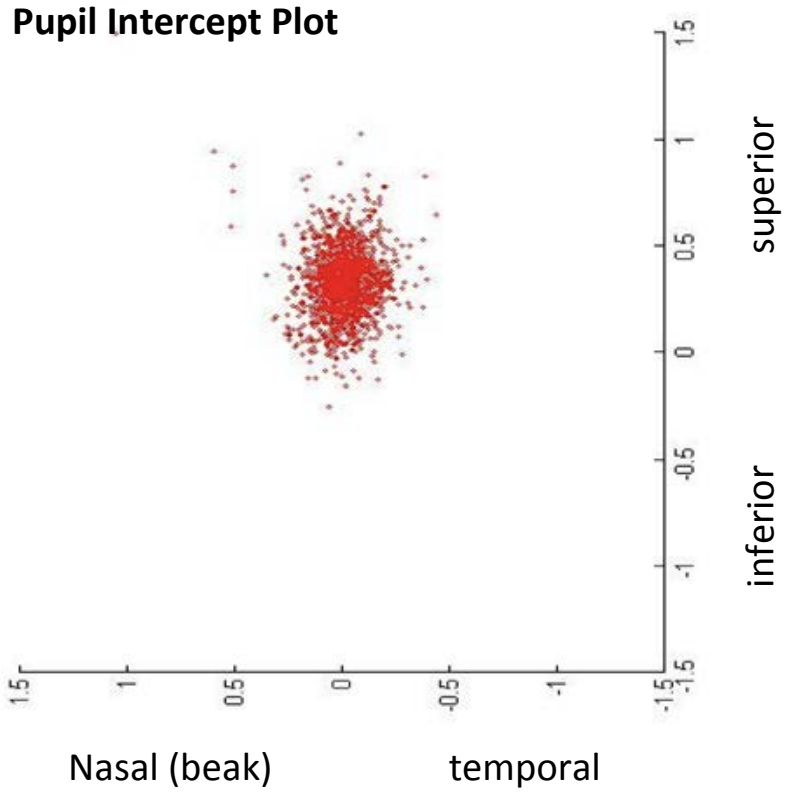

Figure 20. The pupil intercept graph of chick B, measuring 1636 retinal cones' directionality.

In both chick A and B, we see disarray among the cones' directionality, however, this disarray is ultimately quite small. Table 5 shows the displacement of the cone projections from the pupil center and also the fitted σ values from Equation 2. The σ and ρ are related through the equation $\rho = 0.434/2\sigma^2$. We found that all retinal cones generally point toward the same general location on the pupil, slightly superior to the central pupil - Figure 17 and Figure 20.

Subject	Average Cone Directionality (entrance pupil position)		Average angular tuning	
	X peak (mm)	Y peak (mm)	σ	ρ
Chick A	0.222	-0.00122	1.69	0.0756
Chick B	0.327	0.0183	1.86	0.0631

Table 5 The average cone directionalities and angular tuning for both chicks are given above. ρ and σ are related through the equation $\rho = 0.434/2\sigma^2$ The x peak and y peak represent the average pointing direction of the cones.

Discussion

SCE-I can be measured using either a psychophysical (indirect) method or a reflectometric (direct) method. The underlying principle behind reflectometric techniques is that when a cone photoreceptor absorbs light it scatters some back toward the pupil along the same axis as it is positioned. Using this technique, one measures the light reflected back from each cone as it was illuminated through various entrance pupil positions; these measurements were then averaged to determine the directionality of the individual cones within the particular patch of retina being imaged.

Our study uses the multiple-entry reflectometric approach rather than single-entry method where the entrance position of the imaging beam was altered at the subject's pupil plane with the same patch of retina being imaged at each pupil position. In contrast, single-entry reflectometry measures the reflectance of cones from a single beam that traverses the pupil centrally. The ρ values tend to be lower when the multiple-entry reflectometric approach is used as it accounts for peak reflectance from all the cones within the given patch of retina, whereas the single entry approach mainly samples cones that are coaxial to the beam that enters the pupil in the center [46][47].

Our experimental design is modeled off the multiple-entry reflectometry approach of Roorda and Williams [42] for the human eye. They concluded that the tuning function of a large sample of cones is virtually identical to that of a single cone. Our study has similar results, and provides evidence that the cone pointing in chicks is comparable to humans. Their study showed a small overall disarray of cones, similar but slightly less than what we

see in our subjects. Comparison to of our study to that of Roorda and Williams is summarized in Table 6.

Study	Subject	Number of cones (n)	Average cone directionality (entrance pupil position)		Average angular tuning	
			X peak (mm)	Y peak (mm)	σ	ρ
Current study (chicken)	Chick A	973	0.22	-0.001	1.69	0.076
	Chick B	1636	0.33	0.018	1.85	0.063
Roorda & Williams (human)	J.P.	275	1.41	0.194	1.50±0.07	0.096
	G.Y.	200	0.33	0.19	1.66±0.05	0.079

Table 6. Comparison of our findings in the chick eye to the human eye data from Roorda and Williams [42]

COMPARISON WITH OTHER CHICK STUDIES

There has been limited research to date that evaluates the cone directionality in the live chick. The LED study by Beresford et.al.[43] used the psychophysical technique to measure the SCE-I in 3-week-old chicks. Using a and b wave ERG recordings, Beresford calculated "half peak half width" of the waves' (ERG) "peakedness," as well as the displacement of the peak as one moved away from the center of the pupil. They measured at 0.25mm locations across the central 3mm of the pupil, very similarly to what we did. To reach the full pupil margin they also took measurements at the outer 4mm mark. The chickens they imaged were younger than in our experiment, 3 weeks old as opposed to 7 weeks old in our study. In their study they found that photoreceptors in the central 22.5 degrees of the chick retina are generally pointed in a direction approximately 0.22-0.25mm superior (in reference to the pupil center) [43]. This is very similar to what we found, and the pupil intercept graphs show that the majority of our chicks' cones pointed in a direction slightly superior to the

central entrance beam location – Figure 17 and Figure 20. The LED study found that superior cells tend to orient slightly inferior and the inferior cells orient superior (inferior cells with more accuracy). In their paper they did not discuss a quantitative directionality (no angular tuning values), but plotted the Gaussian curves and it can be seen that the curve increases in peakedness at is moves from superior to inferior. As would be expected, the central cells point with relative accuracy. There was a 0.215-0.221 topographical difference in pointing across vertical retina, which simply means that when comparing the cones there was between 21.5% and 22.1% difference in cone direction.

Had they calculated a value of angular tuning we would expect our ρ values to be larger, since previous studies have shown them to be consistently higher for reflectometric measurements than psychophysical measures [46][47].

Conclusion

To our knowledge, this is the first time that individual cone directionality in the living chick eye has been measured directly. Our findings follow the same trend as previously reported in the human eye [42] and show an overall pointing that is consistent with ERG measurements [43].

The expectation is that changes observed in cone directionality can be related to disease. Choi et al. [48] have already shown that cone directionality is affected in a subject with multiple sclerosis (MS). Future work could apply the techniques developed here to avian models of retinal disease.

References

[1] Headington K, Choi SS, Nickla D, Doble N. Single cell imaging of the chick retina with adaptive optics. *Current Eye Research*. 2011; 36(10): 947-957.

[2] DeLint PJ, Berendschot TTJM, van Norren D. A comparison of the optical stiles-crawford effect and retinal densitometry in a clinical setting. *IOVS*. 1998; 39(8):1519-1523.

[3] Birch DG, Sandberg MA. Psychophysical studies of cone optical bandwidth in patients with retinitis pigmentosa. *Vision Res*. 1982; 22:1113-1117.

[4] Birch DG, Sandberg MA, Berson EL. The stiles-crawford effect in retinitis pigmentosa. *IOVS*. 1982; 22:157-164.

[5] Kanis MJ, Wisse RPL, Berendschot TTJM, van de Kraats J, van Norren D. Foveal cone-photoreceptor integrity in aging macula disorder. *IOVS*. 2008;49(5):2077-2081.

[6] Kanis MJ, van Norren D. Delayed recovery of the optical stiles-crawford effect in a case of central serous chorioretinopathy. *Br J Ophthalmol*. 2008;92(2):292-293.

[7] Eckmiller MS. Defective cone photoreceptor cytoskeleton, alignment, feedback, and energetics can lead to energy depletion in macular degeneration. *Progress in Retinal and Eye Research*. 2004; 23:495-522.

[8] Smith VC, Pokorny J, Diddle KR. Color matching and the stiles-crawford effect in observers with early age-related macular changes. *Opt. Soc. Am*. 1988;5(12):2113-2121.

[9] Fitzgerald C.R., Enoch J.M., Campos E.C., Bedell H.E. – Comparison of visual function studies in two cases of senile macular degeneration. *Albrecht V Graefes Arch* 1979; 210: 79-91***

[10] Campos EC, Bedell HE, Enoch JM, Fitzgerald CR. Retinal receptive field-like properties and stiles-crawford effect in a patient with a traumatic choroidal rupture. *Documenta Ophthalmologica*. 1978;45(2):381-395.

[11] Pokorny J., Smith V.C., Johnston P.B. – Photoreceptor misalignment accompanying a fibrous scar. *Arch Ophthalmol.* 1979; 97: 867-869

[12] Yasuma T., Hamer R.D., Lakshminarayanan V., Enoch J.M., O'Donnell J.J. – Retinal receptor alignment and directional sensitivity in a gyrate atrophy patient. *Clin Vision Sci.* 1986; 1: 93-102

[13] Atchinson DA, Scott DH, Strang NC, Artal P. Influence of stiles-crawford apodization

on visual acuity. *Opt. Soc. Am*. 2002;19(6):1073-1083.

[14] Choi SS, Enoch JM, Kono M. Evidence for transient forces/strains at the optic nerve head in myopia: repeated measurements of the stiles-crawford effect of the first kind (SCE-I) over time. *Ophthal. Physiol. Opt.* 2004;24:194-206.

[15] Hart NS, Lisney TJ, Collin SP. Cone photoreceptor oil droplet pigmentation is affected by ambient light intensity. *The Journal of Experimental Biology*. 2006; 209:4774-4787.

[16] Bowmaker JK, Knowles A. The visual pigments and oil droplets of the chicken retina. *Vision Res*. 1977; 17:755-764.

[17] Schaeffel F, Howland HC. Corneal accommodation in chick and pigeon. *Journal of Comparative Physiology*. 1987;160:375-384.

[18] Bedell HE. Central and peripheral retinal photoreceptor orientation in amblyopia eyes as assessed by the psychophysical stiles-crawford function. *IOVS*. 1980;19(1):49-59.

[19] Choi SS, Gamer LF, Enoch JM. The relationship between the stiles-crawford effect of the first kind (SCE-I) and myopia. *Ophthal. Physiol. Opt*. 2003;23:465-472.

[20] Delint PJ, Weissenbruch C, Berendschot TTJM, van Norren D. Photoreceptor function in unilateral amblyopia. *Vision Res*. 1998;38(4):613-617.

[21] Amblyopia and the stiles-crawford effect. *Am J Optom Arch Am Acad Optom*. 1957 Jun;34(6):298-309.

[22] Stiles WS, Crawford BH. Luminous efficiency of rays entering the eye pupil at different points. *Proceedings of the Royal Society of London*. 1933; 112(778): 428-450.

[23] Gorrand J.M. The directionality of photoreceptors in the human retina. *Bull. Soc. Belge Ophthalmol.* 2006; 302:215-229.

[24] O'Brien B. A theory of the stiles and Crawford effect. *Journal of the Optical Society of America*. 1946;36(9):506-509.

[25] Tobaldo di Francia G. Retina cones as dielectric antennas. *Journal of the Optical Society of America*. 1949;39(4):324.

[26] Enoch JM. Optical properties of the retinal receptors. *Journal of the Optical Society of America*. 1963; 53(1): 71-85.

[27] Schaeffel F, Howland HC. Visual optics in normal and ametropic chickens. *Clin. Vision Sci*. 1988; 3(2):83-98.

[28] Meyer DB, May HC. The topographical distribution of rods and cones in the adult chicken retina. *Exp. Eye Res*. 1973; 17:347-355.

[29] Morris VB, Shorey CD. An electron microscope study of types of receptor in the chick retina. *Journal of Comparative Neurology*. 1967;129(4):313-339.

[30] Morris V. Symmetry in a receptor mosaic demonstrated in the chick from the frequencies, spacing, and arrangement of the types of retinal receptor*. Journal of Comparative Neurology.* 1970;140:359-398.

[31] Johnston D, Hudson RA. Isolation and composition of the carotenoid-containing oil droplets from cone photoreceptors. *Biochim Biophys Acta*. 1976; 424(2): 234-45.

[32] Kram YA, Mantey S, Corbo JC. Avian cone photoreceptors tile the retina as five independent, self-organizing mosaics. *PLoS One*. 2010; 5(2): 1-13.

[33] Hart NS, Partridge JC, Cuthill IC. Visual pigments, oil droplets and cone photoreceptor distribution in the European starling (*Sturnus vulgaris*). *J. Exp. Biol*. 1998; 201: 1433-1446

[34] Jones CD, Osorio D. Discrimination of oriented visual textures by poultry chicks. *Vision Res*. 2004;44(1):83-89.

[35] Snyder AW, Pask C. The stiles-crawford effect – explanation and consequences*. Vision Res*. 1973; 13: 1115-1137.

[36] Pallikaris A, Williams DR, Hofer H. The reflectance of single cones in the living human eye. *IOVS*. 2003; 44(10): 4580-4592.

[37] Enoch JM. Waveguide modes: are they present, and what is their possible role in the visual mechanism? *Journal of the Optical Society of America*. 1960;50(10):1025-1026.

[38] Enoch JM. Wave-guide modes in retinal receptors. *Science*. 1961;133:1353-1354.

[39] Enoch JM. Visualization of wave-guide modes in retinal receptors. *Am J Ophthalmol*. 1961;51:1107-1118.

[40] Applegate RA, Bonds BA. Induced movement of receptor alignment toward a new pupillary aperture*. IOVS.* 1981;21:869–872.

[41] Smallman HS, MacLeod DIA, Doyle P. Realignment of cones after cataract removal. *Nature*. 2001;412:604–605.

[42] Roorda A, Williams DR. Optical fiber properties of individual human cones*. Journal of Vision*. 2002; 2:404-412.

[43] Beresford JA, Crewther SG, Crewther DP. A technique for in vivo measurement of photoreceptor orientation in the chicken retina. *Australian and New Zealand Journal of Ophthalmology*. 1999; 27:241-243.

[44] Doble N. High-resolution, *in vivo* retinal imaging using adaptive optics and its future role in ophthalmology. *Expert Rev. Med. Devices*. 2005;2(2):205-216.

[45] Liang J, Grimm B, Goelz S, Bille JF. Objective measurement of wave aberrations of the human eye with the use of a Hartmann-Shack wave-front sensor. *J. Opt. Soc. Am. A* 1994;11(7):1949-1957.

[46] Marcos S, Burns SA, He JC. A model for cone directionality reflectometric measurements based on scattering. *J. Opt. Soc. Am. A* 1998;15:2012-2022.

[47] Marcos S, Burns SA. Cone spacing and waveguide properties from cone directionality measurements. *J. Opt. Soc. Am. A* 1999;16(5):995-1004.

[48] Choi SS, Zawadski RJ, Keltner JL, Werner JS. Changes in cellular structures revealed by ultra-high resolution retinal imaging in optic neuropathies. *IOVS*. 2008;49(5)2103-2119.

Appendix

Poster presented at ARVO 2013

